Complementary Usage of RTI and SfM-MVS for Inspecting Reflective Weld Seams under Water

Oliver Kahmen [1], Thomas Luhmann [1]

[1] Jade University of Applied Sciences, Institute for Applied Photogrammetry and Geoinformatics (IAPG), Ofener Str. 16/19, 26121 Oldenburg, Germany - (Oliver.Kahmen, Thomas.Luhmann)@jade-hs.de

Keywords: Reflectance Transformation Imaging (RTI), Structure from Motion (SfM), Multi-View Stereo (MVS), Underwater Photogrammetry, Lighting, Visual Testing (VT)

Abstract

This article studies the complementary usage of RTI and SfM-MVS visual inspection (visual testing) of welds under water. Two compact low-cost lighting domes of different designs were developed and deployed with a monochromatic camera at close range. The lighting domes generate homogenous and direct illumination, respectively, tailoring the requirements of SfM and RTI. The camera is housed in a cylindrical tube, equipped with a dome port interface. The 3D reconstruction in combination with RTI models could augment existing testing strategies and provide digital, gapless documentation. Experiments were conducted in laboratory in air, clear and turbid water questioning were the capabilities and limits are for given setup with respect to visual testing of welds. Under the correct lightning, in air the techniques perform on a high accuracy level and are well suited for inspecting welds digital and interactively. Underwater the results differ in dependence of the degree of turbidity and prove to be sensitive for configurational parameters leaving space for improvements of acquisition and processing workflows. However, even in turbid water the 3D reconstructions and RTI models could be calculated enabling novel possibilities for weld inspection.

1. Introduction

Photogrammetric techniques, such as Structure from Motion – Multi-View Stereo (SfM-MVS), can produce accurate 3D reconstructions, whereas photometric approaches like Reflectance Transformation Imaging (RTI) mostly aim at visual inspection and documentation.

RTI uses multiple images of varying lighting conditions of direct light to fit reflectance models that can be viewed interactively (Mudge et al., 2006). Small structures can be highlighted and become clearly visible under a certain lighting direction, even if they are smaller than the actual resolving power of the optical system. RTI is common in cultural heritage (Gotsikas et al., 2025) but rarely being used for technical inspection tasks, such as in (Coules et al., 2019), or studied under water as done by (Selmo et al., 2017). In contrast, homogeneous lighting is often used in SfM-MVS pipelines to ensure a visually consistent appearance across the image sequence and to minimise sharp shadows (Mach et al., 2025).

While SfM-MVS generates a 3D pointcloud of multiple viewpoints, RTI calculates a reflectance model at one viewpoint of multiple images. Towards the complementary usage of both techniques some research exists, mostly in field of cultural heritage documentation. In (Pamart et al., 2019), RTI images were co-registered in a web platform to enable interactive illumination in combination with 3D data. The authors of (Morita et al., 2024) incorporated high quality normal maps of RTI to improve 3D reconstructions. In (Richter et al., 2025) images of RTI sequences under varying lighting conditions resp. subsamples of them were used in SfM-MVS pipeline to calculate the surface reconstruction.

In this contribution, the effects of different lighting strategies (direct and indirect) on RTI an SfM-MVS pipelines are analysed to evaluate limits and needs for the application on reflective objects (i.e., welds) under water at harsh environmental conditions. We question if RTI can be used as inspection technique for welds (under water) and study the complementary usage. We use these techniques with different requirements with one single set of low-cost lighting equipment in turbid water.

2. Experimental Setup

In the following the laboratory setup is described. The developed low-cost lighting domes are presented and the calibration and alignment process of the optical system dome port are explained.

2.1 Hardware Setup

For close range visual inspections of welds, test engineers usually use torches to illuminate the object from different angles according to non-destructive testing (NDT) standards such as (ISO, 2017). In this work the torch is, so to speak, replaced by a fixed configuration of numerous single light sources. Two developed low-cost illumination domes were utilised in a laboratory setup in combination with a monochromatic industrial camera mounted in an underwater housing. An aluminium tube of 58mm in (outer) diameter is equipped with a customised dome port; a partial sphere of 69mm in (outer) diameter. The test object is a butt weld with artificially introduced cracks (see Figure 3). These so-called hot cracks were formed due quick cooling after welding. To trigger cracking chopper was introduced at the butt bevor the metal active gas (MAG) welding process. The cracks range from a few microns to ~100µm in width. The weld is ~10mm in width and the probe is 150mm long. In general, for inspecting welds under water (as in air too) a prepared surface, thus cleaned of biofouling, is presumed as usual in visual testing under water.

Figure 1 shows the developed lighting domes. The domes used here are relatively small, mobile and underwater compatible. The (outer) diameter of both domes is ~180mm. The white dome is designed for SfM-MVS. It contains 60 individually controllable LEDs and illuminates the scene indirectly. The light is reflected from the inner of the dome to illuminate the object from every direction to create diffuse and homogenous lighting. In contrast to off-the-shelf dome lights, the LEDs point towards the object, hence the light is reflected from the inner of the dome but also transmitted through a thin diffusor directly towards the object from a flat angle. The black dome is designed for RTI. It contains 18 controllable LEDs, illuminates the scene directly and, due to its black material, barely reflects any indirect light. The LEDs are arranged in three circles of 8/6/4 pieces at three elevation levels. For RTI purposes the direct light from low angles is desirable. Also, for SfM-MVS purposes oblique images are desirable. To fit both needs, the dome was set up ~20mm above the object so that the camera and the attached light dome could be tilted to generate oblique viewpoints but still the LED illuminate from a low angle with respect to the object (see also Figure 4).

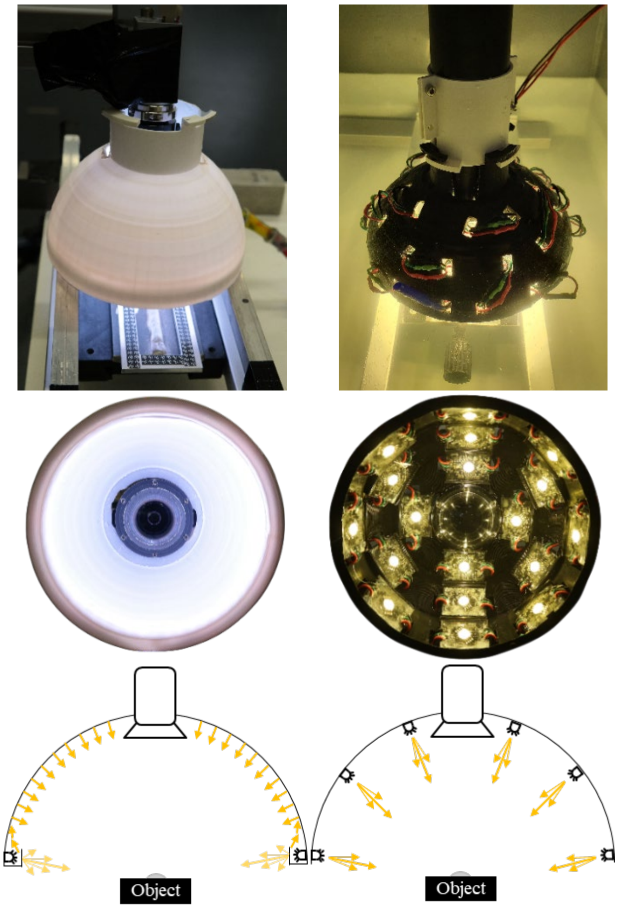

Figure 1. Lighting domes. Left column: white dome. Right column: black dome. Top row: domes observe weld, exemplarily in air (left) and in water (right). Centre row: light domes from downside with centred camera pointing towards the viewer. Bottom row: sketch of light positions, directional vectors and reflections.

2.2 Alignment and Calibration

The alignment of the dome ports centre and entrance pupil is critical in underwater photogrammetry in order to use the standard single-media photogrammetric model (Menna et al., 2016; She et al., 2019). To align the entrance pupil to the dome port the camera is centred in the cylindrical housing. Thanks to the customised, transferable mount in the tube, the camera is moved along the optical axis in order to achieve the alignment via the half-half-technique after (She et al., 2019). A simple plastic box with a silicone sealed feed-through serves as an alignment tank, so that the cylindrical underwater housing can be inserted without leaking (see Figure 2). While being half underwater the camera can be aligned inside the housing easily from the open backside of the cylinder.

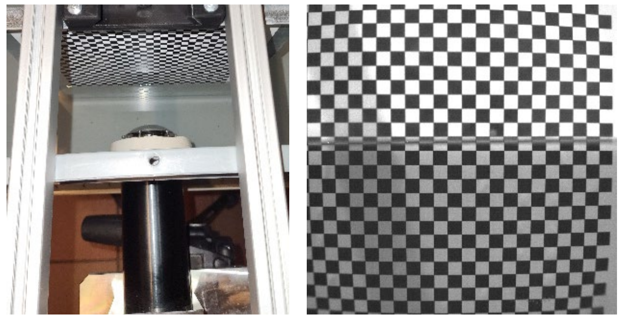

Figure 2. Left: top view of the camera tube penetrating the water basin. The camera is on the water-surface-level observing a chessboard target through the hemispheric interface. Right: camera image of the chessboard half in water half in air.

Since the linear geometry of image sequences along a weld are non-collaborative in terms of a self-calibrating bundle adjustment (Luhmann et al., 2023), the interior camera parameters were pre-calibrated and introduced as fixed parameters to the SfM-MVS process. The interior parameters of the optical system were determined using a 3D calibration fixture consisting of ~160 points of 1mm in diameter. The calibration was carried out underwater with the mounted dome port, while for the in-air datasets no dome port was mounted during calibration and further image acquisition.

The calibration of the directional vectors of light, as necessary for RTI, was conducted placing two spheres in the scene (see Figure 9) in order to calculate the directional vector of light as described in (Mudge et al., 2006). The calibration was done before each experimental dataset to make sure the relation of camera and LEDs is correct, since the lighting domes were switched between the experiments.

3. Methodology and Datasets

Different datasets were acquired in a controlled environment under a varying degree of turbidity to study the effect of lighting with respect to the application of visual inspection. The MAG butt joint serves as main test object.

3.1 Reference

The reference data of the butt joint was acquired in air using a Nikon D850 + 35mm lens and homogenous lighting of a light tent. The reference pointcloud features a spatial resolution of 0.03mm at a mean reprojection error of 0.3 pixel.

Figure 3. Top: test object, region of interest (ROI) is marked red. Bottom left: perspecitve view of the reference pointcloud in the ROI without texture. Bottom right: as left with texture.

For the reference data, circular targets with known geometry have been placed around the weld generously to support the bundle adjustment and provide scaling. In the experimental datasets reference markers on a magnetic frame support the linear configuration and provide scale (see Figure 4 and Figure 5).

3.2 Experimental Datasets

In practice, the camera is supposed to be moved along the weld. For simplification of the experimental setup, here the weld was slid linearly under the camera and the lighting dome for easier image acquisition. Figure 4 visualises the acquisitional principle. Three acquisition lines were recorded resulting in an image sequence of around 3x80 images per experiment for inspecting the 150mm weld seam. One nadir and two oblique lines were acquired. Due to hardware restrictions and the limited depth of field of ~20mm at 2 pixel circle of confusion, the configuration is similar to a nadir aerial imaging setup. At three positions from top view, besides regular images, the RTI acquisition process was utilized. At these positions along the weld, 30 (white dome) resp. 18 (black dome) images were acquired under varying illumination. In this work an overlap of 20% from one RTI spot to the next was applied. Following equation 1, the needed distance between RTI acquisition spots can be calculated simply according to the needs of the application for linear welds. For comparison of the ROI, the RTI at position 2 have been analysed.

$$RTI_{adist} = \frac{h}{c} \cdot S_{width} \cdot o \qquad (1)$$

where h = acquisition height
c = principal distance
S_{width} = width of the sensor
o = overlap

The main analysis is based on 12 datasets. Six datasets were acquired using the white homogenous lighting dome and six with the black direct lighting dome. The experiments are listed in Table 1. According to the nomenclature, the first dataset represents the data acquired with the white homogenous lighting dome applied in air with no turbidity present. Four different turbidity level (tl1-4) have been realised, tl0 represents clear tap water. The turbidity has been created mixing Maaloxan® with the water. As suggested by (Stephan, 2016) applying Maaloxan® can establish controllable turbidity conditions. The utilized portions (see percentage of Maaloxan® in Table 1) are identical with the turbidity levels 2,4,6,8 in (Kahmen and Luhmann, 2022).

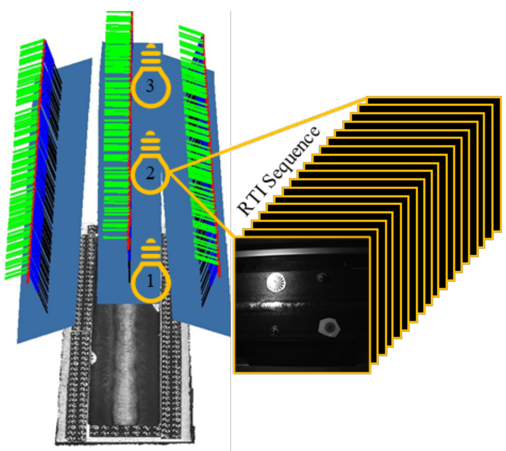

Figure 4. Acquisition principle. Three lines of approx. 80 images were taken under stable lighting. At three positions RTI sequences of 30 (white dome) resp. 18 (black dome) images were recorded under varying illumination.

w_air	b_air	
w_water_0	b_water_0	tl0 → 0.000%
w_water_1	b_water_1	tl1 → 0.015%
w_water_2	b_water_2	tl2 → 0.045%
w_water_3	b_water_3	tl3 → 0.075%
w_water_4	b_water_4	tl4 → 0.105%

Table 1. Experimental datasets and turbidity levels. The nomenclature is *lighting dome_medium_turbidity level*.

4. Analysis

The analysis of the data is separated in 4 subsections. At first, images of the datasets of Table 1 for the SfM-MVS processing are analysed. Here, only images acquired under constant lighting are taken into account. Next, the corresponding SfM-MVS results are presented before the RTI datasets are evaluated. Last the complementary usage of SfM-MVS and RTI is analysed.

4.1 Image Analysis

For image analysis of images under constant illumination (all LEDs activated) only the region of interest (see Figure 3) was evaluated in order to compare only a relevant part of the images, whose parameters are not falsified by the global image. Thus, global artifacts due to imperfect alignment of compared images or histogram artefacts due to image parts outside the ROI are excluded in the analysis. In general, the images were acquired at different exposure times, due to the different luminance intensity of the two lighting domes and due to higher light absorption and backscattering in more turbid water. Since the object was slid under the camera, the compared images of different datasets are not taken at the exact same position either. However, the brightness of the images acquired (see Figure 5) was tried kept homogenous throughout the datasets by levelling the white parts at the image center (at the circular targets) to be just at the edge of being overexposed. For simplification, only four of six datasets are presented in the following.

As valid for all datasets, due to positional and perspective differences, the images cannot be compared pixelwise. However, non-pixelwise metrics with regard to the ROI are presented in Table 2. Besides the mean value and contrast, the ratio of saturated pixels is given, quantifying the specular reflections. In the full-size original images, the reflections of the direct light of the black dome can be observed, while, in the homogenous illuminated image, the reference frame and targets as well as the weld itself appear softer. In none of the ROI-images under homogenous lighting saturated pixels are present. The images in air and in clear water hardly differ from one another for both domes. Increased turbidity reduces the contrast that is higher in general for the direct lighting (see Table 2), what also reduces the range of the grey values in the histograms (see Figure 6).

The contrast was calculated as RMS-contrast, thus less sensitive for extreme values (specular reflexions) and can be calculated as follows.

$$C_{RMS} = \sqrt{\frac{1}{N}\sum_{i=1}^{N}(I_i - \bar{I})^2} \qquad (2)$$

where I_i = grey value of an individual pixel
$\bar{I}$ = mean value of all pixels

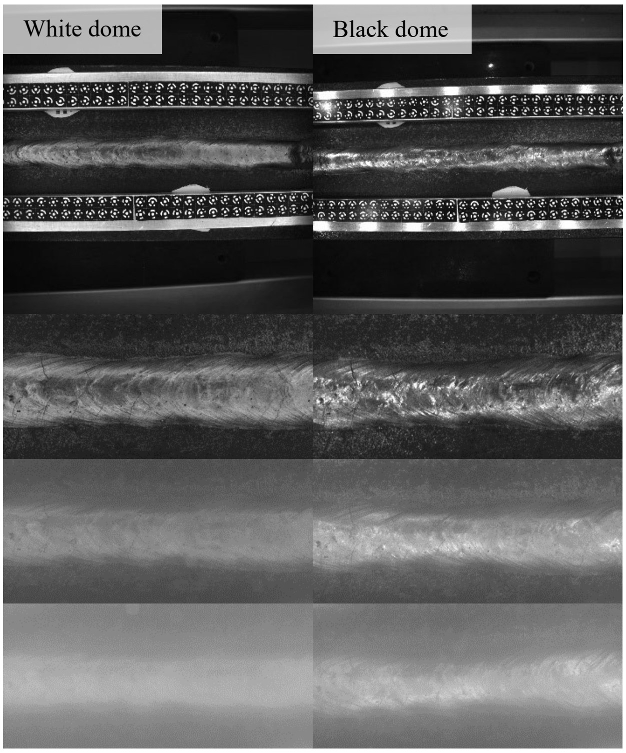

Figure 5. Left column represents images taken under homogenous light (white dome). Right column represents images taken under direct light (black dome). Top to bottom: full-size image with magnetic reference frame next to the weld. ROI in air, ROI in tl2, ROI in tl4.

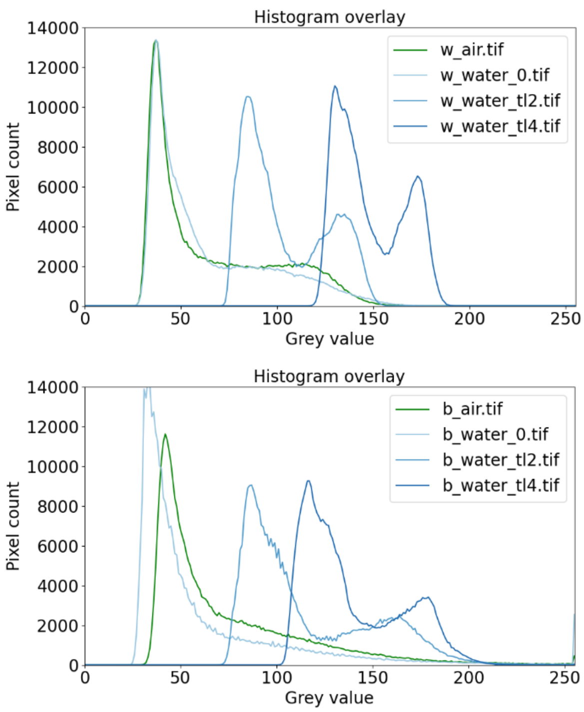

Figure 6. Top: histograms the ROI of white dome experiments. Bottom: histograms of the ROI of black dome experiments.

4.2 SfM-MVS

The images of the datasets (see Table 1) were processed in Agisoft Metashape (Version 2.0.3) to calculate 3D data of the weld geometry. The reference targets on the frame were introduced as weighted reference points. The pre-calibrated interior orientation of the camera was introduced as fixed. Before alignment, the images were masked circularly with 7/8 of the image width (=height) in diameter to exclude image boarders. After camera alignment, and a standardised tie point cleaning, the dense point and metrics were calculated for further analysis (see Table 2). A strict processing workflow and explanations on filtering methods are provided by (Di Filippo et al., 2022). Here, the alignment and dense cloud were calculated in *high*, hence full resolution was used for calculation.

Standardised tie point cleaning after alignment:

1. Filter points outside reference frame
2. Filter worst 10% after reconstruction uncertainty
3. Optimise cameras
4. Filter worst 10% after projection uncertainty
5. Optimise cameras
6. Filter worst 3% after reprojection uncertainty
7. Optimise cameras
8. Calculate dense cloud and export metrics

The inner of the frame represents the weld and the head-affected zone around it, which are of interest for visual inspection, hence used for 3D analysis. Due to the standardised workflow obtained results might not be the possible bests for the dataset, therefore, all datasets become comparable throughout the experiments.

The 3D data of the experiments were registered with the reference data via iterative closest point (ICP) algorithm. The metrics in Table 2 evaluate the quality of the reconstruction.

The root mean square error (RMSE) of the reference points describe the residuals of those. There is barely a difference, but, probably due to better calibration and no interface being part of the optical system, the in-air sets are of higher accuracy indicating a more constraint-free datum of the network. The reprojection error represents the inner accuracy and includes the image degradation due to optical components (dome port is critical), thus again is better in air datasets. S_{xyz} indicates the absolute accuracy as a comparison *Cloud2Mesh* with the reference data after ICP.

It can be seen that the degree of degradation of the quality is much higher starting at a high-quality level for white dome data. All black dome data are of similar quality regarding the geometry. However, as presented in Figure 7, the data contain many data gaps and noise. By evaluating the roughness and density this imperfection can be quantified indirectly in addition. Here the roughness describes the deviation of a best-fitting plane within a radius of 0.3mm (approx. 3x3 object points) and the density counts all points in a sphere of 1mm (mean values are given in Table 2). Seeing 116 points at the best dataset (w_air), much more points observed in datasets of turbidity indicate a higher noise at the surface. Again, the difference between the datasets, thus the sensitivity for turbidity, is less for black dome data.

https://doi.org/10.5194/isprs-archives-XLIX-B2-2026-947-2026 |

Dataset	Image (ROI)			Geometry (pointcloud)							RTI
	Mean	$Contrast_{RMS}$	Sat. Pixel [%]	Tie Points after filtering	Avg. Projections/ Image	Ref. Points RMSE [mm]	Reprojection Error [px]	S_{xyz} [mm]	Roughness r = 0,3 [mm]	Density r = 1mm [mm]	HSH
w air	66	32	0	97.444	2411	0.005	0.32	0,03	0,009	116	✓
w water 0	64	31	0	101.938	2342	0.010	0.50	0,06	0,013	117	✓
w water tl2	104	22	0	65.606	1311	0.012	0.61	0,10	0,012	126	✓
w water tl4	148	18	0	35.550	560	0.010	0.73	0,30	0,030	184	✓
b air	74	39	0,13	90.229	1153	0.005	0.41	0,19	0,018	112	✓
b water 0	61	41	0,74	99.465	1380	0.010	0.53	0,09	0,012	115	✓
b water tl2	116	33	0,02	80.726	1289	0.010	0.57	0,17	0,130	120	✓
b water tl4	139	25	0,00	56.124	732	0.010	0.66	0,19	0,140	125	✓

Table 2: Analysis of the datasets. Image metrics and geometry metrics. RTI indication of HSH model calculation.

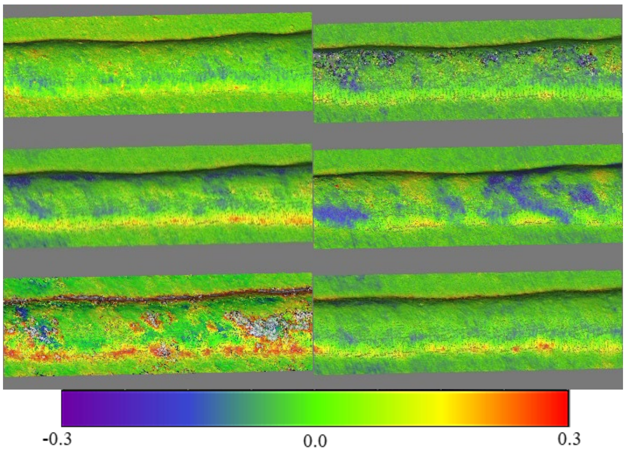

Figure 7. Deviation from reference. S_{xyz}. From left to right: Top: w_air, b_air. Centre: w_water_tl2, b_water_tl2. Bottom: w_water_tl4, b_water_tl4.

4.3 RTI

Besides images underlying constant illumination used for SfM-MVS, image sequences at certain positions were acquired under varying lighting conditions (see Figure 4). These images build the base for the RTI processing, which was executed as hemispherical harmonics (HSH) model in the software *Relight* (Version 2025.12), since HSH is better suited for reflective materials (MacDonald, 2015).

The lighting dome setups are non-optimal for RTI proposes in terms of distribution, number and arrangement of the LEDs. Furthermore, the turbidity degrades the image quality, so that it was questionable if (reasonable) RTI models could be calculated at all. Table 2 lists, if the calculation of an RTI model was possible in general using HSH. All datasets could be processed to an RTI model. Only at w_water_tl4 manually calibrating the directional vector of lights was necessary due to blurry and dark light reflections in the calibration spheres. Since the light only varies in azimuth and no elevational change is present, white dome models are interpolated poorly when the rendered interactively, even though the HSH calculation still was possible. The interaction is highly sensitive for elevational change of virtual light position but still works in general. In case of the black dome, the interpolation of the rendering is, due to its varying light elevation, much better. Therefore, the interactivity is of higher comfort and less sensitive. Figure 8 illustrates the accumulated light positions detected in individual images.

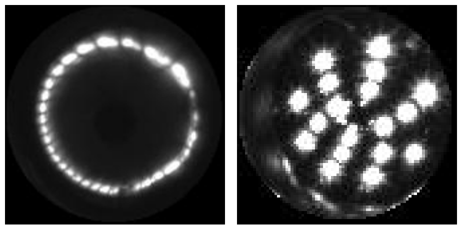

Figure 8. Accumulated highlight reflections of white dome (left) and black dome (right) in one of the two calibration spheres.

The images and results are barely comparable on a quantitative level, since the images are highly sensitive for the position of the optical sensor and the LEDs. Furthermore, the exposure time for single LEDs illuminating the scene needed to be much higher compared to constant lighting conditions when all LEDs were active. The longest exposure in dataset w_water_tl4 was about 1/7 sec. for a single image. At 30 images, the camera-object relation would need to be stable for >4 seconds, which is impossible for a handheld system without mechanical guidance, especially in harsh environments as under water.

Figure 9 exemplarily shows the calibration images of the two lighting domes. Two spheres were used. The effects regarding degradation, exposure times and specular reflections are similar as observed for images under constant illumination within the ROI (see section 4.1).

On a qualitative level it can be observed that the interactivity of RTI models of the black dome data is much more convenient. However, since the white dome consists of 30 images around a circle, while the black only features 8/6/4 in each elevation, when inspecting the weld at a certain level of evaluation, the white dome offers gapless data. The interpolation is poor in azimuth for the black dome, while it is poor in elevation for the white dome. Furthermore, it can be observed that the RTI model does not create extra data; therefore, what is not visible in the image sequence won’t be visible in the RTI model. However, it creates extra (interactive) visualisation possibilities which can be useful for (digital) visual inspection.

This contribution has been peer-reviewed.
https://doi.org/10.5194/isprs-archives-XLIX-B2-2026-947-2026

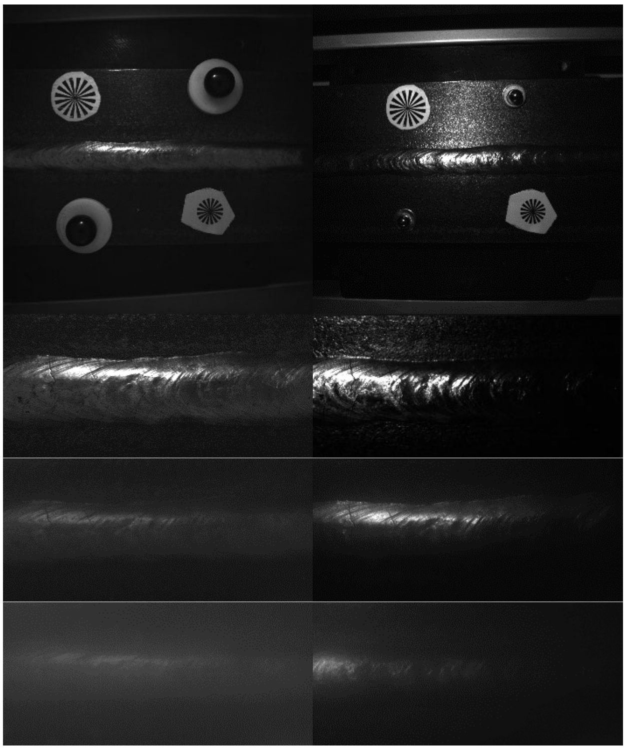

Figure 9. Left column represents images with white dome. Right column represents images taken under direct light (black dome). From top to bottom: full-size image, ROI in air, ROI in tl2, ROI in tl4.

Figure 10 shows rendered images of the RTI model compared to the regular images under constant lighting. Due to the tendency of producing overexposed regions, direct light as strong and close to the object as in the presented application might lead to loss of information. Depending on what detail is of interest (crack, weld toe, main material, pores, surface pattern, etc.) one image may be more suitable than another for visual inspection. The main advantage of using RTI instead or as an extra to regular images is, that weld defects and structures can be highlighted interactively tailored to the needs of inspection.

Exemplarily, Figure 11 visualises two interactively created renderings of a butt (white lighting dome) and a hollow weld (handheld torch) that could be used for semi-automated digital visual testing. The first highlights the width of the butt weld used in the experiments in this work. The second rendering highlights weld spatter and the irregular weld transition of a hollow weld.

The turbidity flattens the image so that the tendency to overexposure the highly reflective steel when direct light is applied decreases at increasing turbidity level. This reciprocal relationship depends on the kind of turbidity and the lighting being applied. Since in this work the suspended particles reflect whitely, the light of the domes is of full spectrum (white LED light) and monochromatic cameras are used the reciprocal relationship of flattening appears stronger than in real world scenarios. In air or at low turbidity levels the white dome images are well suited for inspection purposes, while the RTI models are too sensitive for practical usage. Due to the homogenous character of the white dome, the light illuminates the object but also particles from all directions resulting in strong flattening effect with increasing turbidity. In contrast, the black dome images and RTI models have their strength at higher turbidity levels and tend to loss information due to specular reflections in air respectively less turbid water.

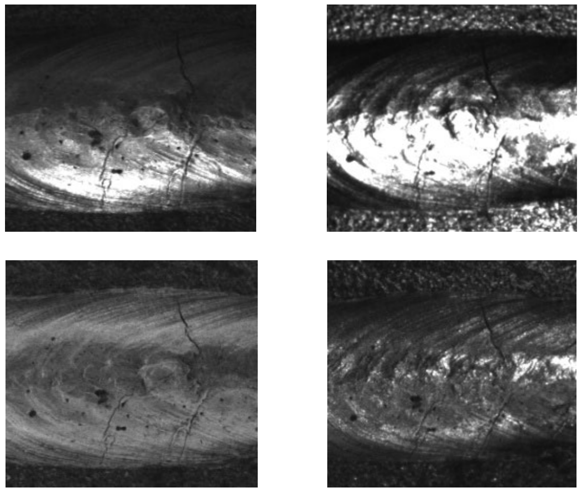

Figure 10. Top row: detail rendering of RTI model from white dome (left) and black dome (right). Bottom row: detail of image under constant light of white dome (left) and black dome (right).

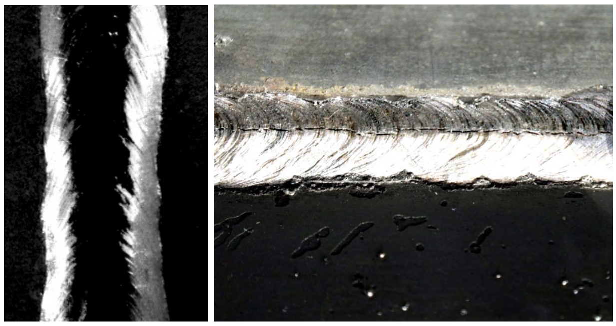

Figure 11. Examples of RTI renderings. Left: the width of a butt weld is highlighted. Right: weld spatter and lower weld transition of a hollow weld are highlighted.

4.4 Complementary Usage

Both, SfM-MVS and RTI have their advantages and challenges with respect to the task of visual inspection of welds under water. The 3D data is well suited to measure different defect criteria according to applicable standards (ISO, 2023). However, the 3D pointcloud exhibits a low-pass filtering-like effect, which prevents details (e.g., cracks or pores) from being resolved geometrically. The texture of a pointcloud might feature these details, which is a main advantage of image-based measuring systems over laserline-based ones in terms of visual inspection. However, the texture still appears blended depending on the quality of the bundle and loses information due to poor image quality; underwater, intensified by backscattering.

RTI is a valuable addition to SfM-MVS similar to the real-world visual inspection using a moved torch. The interaction by controlling the virtual movement of the light source is fascinating. The complementary usage becomes more valuable when RTI models are oriented within the bundle.

The RTI image sequences were oriented within the image bundle by acquiring one regular illuminated image at the position of each RTI spot. This image served as part of the SfM-MVS pipeline and provided orientation parameters for the RTI sequence at the same time. When oriented, RTI renderings (e.g., as in Figure 11) as well as original images of the RTI sequence under varying illumination can be used to conduct 2D measurements. Depending on the overlap of RTI sequences (see section 3.2) inspection criteria can be measured in ≥ 2 RTI sequences, thus being forward intersected to calculate 3D points. If just one RTI sequence is available to inspect a certain detail, what would be more practical, the rendered image can still be used to measure a point. The spatial vector defined by the 2D image measurement can then be projected onto the calculated 3D pointcloud resulting in an intersection Point **P**.

$$\boldsymbol{P} = \boldsymbol{P_0} + \frac{\boldsymbol{n}^T(\boldsymbol{S}-\boldsymbol{P_0})}{\boldsymbol{n}^T\boldsymbol{r}} \cdot \boldsymbol{r} \tag{3}$$

with **r** being the directional vector

$$\boldsymbol{r} = \boldsymbol{R} \cdot \begin{pmatrix} x' \\ y' \\ c \end{pmatrix} \tag{4}$$

where $\boldsymbol{P}$ = spatial intersection point
x', y' = undistorted image coordinates
$\boldsymbol{n}$ = normal vector of the local planar surface
$\boldsymbol{S}$ = point on pointcloud surface
$\boldsymbol{P_0}$ = projection center
r = directional vector
c = principal distance
R = rotation matrix of the camera

Rather than applying full error propagation to equation, a simplified model can be employed, assuming the object is oriented parallel to the image plane. The lateral error (X,Y) within the local object plane of the intersection point **P** can be calculated by equations 5 and 6, while the error along the surface normal (Z), is defined by the quality of the pointcloud (equation 7).

$$\sigma_X = \sqrt{\left(\frac{h}{c} \cdot \sigma_{x'}\right)^2 + (\sigma_Z \cdot tan\,(\alpha))^2} \tag{5}$$

$$\sigma_Y = \sqrt{\left(\frac{h}{c} \cdot \sigma_{y'}\right)^2 + (\sigma_Z \cdot \tan\,(\alpha))^2} \tag{6}$$

$$\sigma_Z = \sigma_{surf,n} \tag{7}$$

where h = acquisition height
$\sigma_{x',y'}$ = error of image measurement
$\sigma_{surf,n}$ = error in local plane along its normal
α = incidence angle

Assuming $\sigma_{x',y'}$ of 1 pixel, the reachable precision in XY-plane at the surface is ~ 48 to 53µm (image centre to edge of image at $\alpha = 25°$) for the here presented experiments at h ≈ 95mm and c ≈ 11mm. The precision normal to the surface depends on the reconstruction quality only and is assumed as $\sigma_{surf,n}$ = 50µm.

Especially for specular surfaces, RTI models might contain inaccuracies leading to false shadow rendering (Drew et al., 2012). Thus, when 2D measurements are taken in the RTI renderings, these inaccuracies might downgrade the precision.

Geometric assessment for some defects is of minor interest since they are not permitted anyway. As an example, when a crack is identified as such, its parameter are irrelevant since the weld will be classified as unacceptable (not valid for micro cracks according to (ISO, 2023)). For other testing relevant characteristics (e.g., pores), the geometry is of interest to classify the weld according to limit values of classes B, C and D.

5. Discussion

5.1 Practical Observations

RTI can be conducted using a moved light (e.g., torch) or fix framed lightning domes as in this contribution. In terms of practical usage both would be suitable for underwater weld inspection but a fixed frame has two main advantages over handheld lighting devices. First, acquisition can be speed up. The developed low-cost black dome operates at 5V and costs <100€. Due to short distances (light and camera) even in turbid water the exposure time could be kept short (1/100 at black_water_tl4), hence the frame rate of the camera is the bottleneck regarding speed. At 30Hz, 18 frames could be acquired in 0.6 seconds. Using a torch would take several seconds in which the camera-object relation must be stable. Second, when a fixed LED dome is utilised, the spheres (at least one) for calibrating the directional light vectors do not have to be present in-situ. As long as the relation of camera and light vectors is calibrated once and physically fixed, the calibration stays valid, which is a high value for non-laboratory RTI applications.

We found that SfM-MVS is sensible for specular reflections, even with high redundancy image sequences due to imperfect image matching. Also, when RTI models are created, saturated pixels tend to be present at direct lighting from short range degrading inspection possibilities due to loss of information. However, when the light configuration is well suited for RTI/SfM-MVS purposes with respect to present water conditions, both techniques work well for weld inspection. The 3D reconstruction process can be automated to a high degree using off-the-shelf software with additional scripts.

5.2 Capabilities, Needs and Limits of RTI, SfM-MVS and their Complementary Usage

This contribution presents a challenging application in close range photogrammetry under water targeting reflective objects and high resolution. Restrictions regarding the hardware setup are given by space constrains, limited visibility, limited depth of field and necessity of light power. When conducting RTI and SfM-MVS these restrictions are even more challenging, since both techniques have contrary requirements. In general, it is possible to reach high accuracy reconstructions and reasonable RTI models for complementary usage for visually inspecting welds under water with low-cost lighting equipment. However, the configuration for RTI and SfM-MVS is sensitive, especially for specular reflections, and needs to be suited for the desired application. This sensitivity could be reduced by hardware optimisations creating further requirements. First, only a certain wavelength of light could be used to reduce dispersion, thus blurry images and calibration uncertainties. More power and/or longer exposure times would be needed. Second, the shadow of the camera could be kept small using a miniaturised camera and optimised lighting dome aperture.

Additionally, filtering images can improve 3D reconstructions for low contrast images (Vrochidis et al., 2025). Image filtering for RTI modelling is an open research question.

The usage of RTI and 3D reconstruction in one setup is reasonable since the techniques complement each other and RTI can fulfil many needs of testing standards (identifying rather than measuring).

6. Conclusion

Experiments show that the proposed setup is capable to reconstruct a weld surface and additionally provide RTI models in high quality in air. However, the challenging non-collaborative, configurational and environmental setups (illumination, specular object, limited acquisition geometry, turbidity) made it difficult to reach high levels of completeness and accuracy in underwater datasets. RTI proves to be a great technique, so to speak as virtual torch, to be applied for weld inspection tasks even though it has limited possibilities and special needs when applied under given conditions. The interactive possibility of visual inspection and further image measurements complement the 3D data in a meaningful way.

In air the complementary usage of SfM and RTI could become a digital standard in process chains for documentation and preservation of evidence. Applied under water, this statement is much more sensitive for environmental and configurational restrictions but could also be valid.

Future work will investigate how the illumination wavelength can support reconstruction and RTI processing in turbid waters in combination with filtering algorithms to make better use of the proposed system. Furthermore, a combination of light sources differentiating the needs for both techniques could be deployed. In terms of VT testing relevant geometries could be separated in classes *identification* and *measuring* to test those with regard to both, RTI and SfM-MVS processing.

Acknowledgement

This work is based on a project, funded by the Federal Ministry for Economic Affairs and Energy (IGF-Project 01IF22587N).

References

Coules, H.E., Orrock, P.J., Seow, C.E., 2019. Reflectance Transformation Imaging as a tool for engineering failure analysis. Engineering Failure Analysis 105 (4), 1006–1017.

Di Filippo, A., Antinozzi, S., Dell'Amico, A., Sanseverino, A., 2022. A STATISTICAL ANALYSIS FOR THE ASSESSMENT OF CLOSE-RANGE PHOTOGRAMMETRY GEOMETRICAL FEATURES. Int. Arch. Photogramm. Remote Sens. Spatial Inf. Sci., XLVIII-2/W2-2022, 31–38.

Drew, M.S., Hel-Or, Y., Malzbender, T., Hajari, N., 2012. Robust estimation of surface properties and interpolation of shadow/specularity components. Image Vis. Comput. (30), 317–331.

Gotsikas, I.N., Tzifopoulos, Y.Z., Mitkas, P.A., 2025. Digital Ektypon: Using an RTI Dome for Digitizing Squeezes and Epigraphic Research. IEEE Access 13, 25154–25162.

ISO, 2017. ISO 17637:2016. Non-destructive testing of welds - Visual testing of fusion-welded joints.

ISO, 2023. ISO 5817:2023. Welding - Fusion-welded joints in steel, nickel, titanium and their alloys (beam welding excluded) - Quality levels for imperfections.

Kahmen, O., Luhmann, T., 2022. Monocular Photogrammetric System for 3D Reconstruction of Welds in Turbid Water. PFG (90), 19–35.

Luhmann, T., Robson, S., Kyle, S., Boehm, J., 2023. Close-Range Photogrammetry and 3D Imaging, 4th edition. De Gruyter, Berlin.

MacDonald, L.W., 2015. Representation of Cultural Objects by Image Sets with Directional Illumination. In: Trémeau, A., Schettini, R., Tominaga, S. (Eds.), Computational Color Imaging. Springer International Publishing, Cham, 43–56.

Mach, J., Svatý, Z., Šoupa, O., Nouzovský, L., Halecký, M., 2025. Implementation of an SfM-MVS-based photogrammetry approach for detailed 3D reconstruction of plants. Plant methods 21 (1), 127.

Menna, F., Nocerino, E., Fassi, F., Remondino, F., 2016. Geometric and Optic Characterization of a Hemispherical Dome Port for Underwater Photogrammetry. Sensors (Basel, Switzerland) 16 (1), 48–68.

Morita, M.M., Loaiza Carvajal, D.A., González Bagur, I.L., Bilmes, G.M., 2024. A combined approach of SFM-MVS photogrammetry and reflectance transformation imaging to enhance 3D reconstructions 68, 38–46.

Mudge, M., Malzbender, T., Schroer, C., Lum, M., 2006. New Reflection Transformation Imaging Methods for Rock Art and Multiple-Viewpoint Display. The Eurographics Association.

Pamart, A., Ponchio, F., Abergel, V., Alaoui M'Darhri, A., Corsini, M., Dellepiane, M., Morlet, F., Scopigno, R., Luca, L. de, 2019. A COMPLETE FRAMEWORK OPERATING SPATIALLY-ORIENTED RTI IN A 3D/2D CULTURAL HERITAGE DOCUMENTATION AND ANALYSIS TOOL. Int. Arch. Photogramm. Remote Sens. Spatial Inf. Sci., XLII-2/W9, 573–580.

Richter, J.-N., Kahmen, O., Rofallski, R., Luhmann, T., Chizhova, M., Albers, S., 2025. Reflectance Transformation Imaging for Detecting Knots in Heritage Timbers. Int. Arch. Photogramm. Remote Sens. Spatial Inf. Sci., XLVIII-M-9-2025, 1289–1294.

Selmo, D., Sturt, F., Miles, J., Basford, P., Malzbender, T., Martinez, K., Thompson, C., Earl, G., Bevan, G., 2017. Underwater reflectance transformation imaging: a technology for in situ underwater cultural heritage object-level recording. Journal of Electronic Imaging 26 (01), 1.

She, M., Song, Y., Mohrmann, J., Köser, K., 2019. Adjustment and Calibration of Dome Port Camera Systems for Underwater Vision. In: Fink, G.A., Frintrop, S., Jiang, X. (Eds.), Pattern Recognition. 41st DAGM German Conference, DAGM GCPR 2019, Dortmund, Germany, September 10–13, 2019, Proceedings, 1.th ed. Springer, Cham, 79–92.

Stephan, T., 2016. Beitrag zur Unterwasserbildrestauration. Dissertation, http://nbn-resolving.de/urn:nbn:de:0072-585672.

Vrochidis, A., Tzovaras, D., Krinidis, S., 2025. Enhancing 3D Reconstructions in Underwater Environments: The Impact of Image Enhancement on Model Quality. Int. Arch. Photogramm. Remote Sens. Spatial Inf. Sci. XLVIII-2/W10-2025, 317–324.